

# Near-unity nuclear polarization with an open-source $^{129}\text{Xe}$ hyperpolarizer for NMR and MRI

Panayiotis Nikolaou<sup>a,b</sup>, Aaron M. Coffey<sup>a,c</sup>, Laura L. Walkup<sup>b</sup>, Brogan M. Gust<sup>b</sup>, Nicholas Whiting<sup>d,1</sup>, Hayley Newton<sup>d</sup>, Scott Barcus<sup>b,e</sup>, Iga Muradyan<sup>f</sup>, Mikayel Dabaghyan<sup>f</sup>, Gregory D. Moroz<sup>g</sup>, Matthew S. Rosen<sup>h,i</sup>, Samuel Patz<sup>f</sup>, Michael J. Barlow<sup>d</sup>, Eduard Y. Chekmenev<sup>a,c,j</sup>, and Boyd M. Goodson<sup>b,2</sup>

<sup>a</sup>Department of Radiology, Vanderbilt University Institute of Imaging Science, Nashville, TN 37232; <sup>b</sup>Department of Chemistry and Biochemistry, Southern Illinois University, Carbondale, IL 62901; <sup>c</sup>Department of Biomedical Engineering, Vanderbilt University, Nashville, TN 37235; <sup>d</sup>Sir Peter Mansfield Magnetic Resonance Centre, University of Nottingham, Nottingham NG7 2RD, United Kingdom; <sup>e</sup>Department of Physics, Drake University, Des Moines, IA 50311; <sup>f</sup>Brigham and Women's Hospital and Harvard Medical School, Boston, MA 02115; <sup>g</sup>Graduate School Central Research Shop, Southern Illinois University, Carbondale, IL 62901; <sup>h</sup>Department of Physics, Harvard University, Cambridge, MA 02138; <sup>i</sup>Massachusetts General Hospital/Athinoula A. Martinos Center for Biomedical Imaging, Boston, MA 02129; and <sup>j</sup>Department of Biochemistry, Vanderbilt University, Nashville, TN 37205

Edited\* by Alexander Pines, University of California, and Lawrence Berkeley National Laboratory, Berkeley, CA, and approved July 23, 2013 (received for review April 8, 2013)

The exquisite NMR spectral sensitivity and negligible reactivity of hyperpolarized xenon-129 ( $\text{HP}^{129}\text{Xe}$ ) make it attractive for a number of magnetic resonance applications; moreover,  $\text{HP}^{129}\text{Xe}$  embodies an alternative to rare and nonrenewable  $^3\text{He}$ . However, the ability to reliably and inexpensively produce large quantities of  $\text{HP}^{129}\text{Xe}$  with sufficiently high  $^{129}\text{Xe}$  nuclear spin polarization ( $P_{\text{Xe}}$ ) remains a significant challenge—particularly at high Xe densities. We present results from our “open-source” large-scale ( $\sim 1$  L/h)  $^{129}\text{Xe}$  polarizer for clinical, preclinical, and materials NMR and MRI research. Automated and composed mostly of off-the-shelf components, this “hyperpolarizer” is designed to be readily implementable in other laboratories. The device runs with high resonant photon flux (up to 200 W at the Rb D<sub>1</sub> line) in the xenon-rich regime (up to 1,800 torr Xe in 500 cc) in either single-batch or stopped-flow mode, negating in part the usual requirement of Xe cryocollection. Excellent agreement is observed among four independent methods used to measure spin polarization. In-cell  $P_{\text{Xe}}$  values of  $\sim 90\%$ ,  $\sim 57\%$ ,  $\sim 50\%$ , and  $\sim 30\%$  have been measured for Xe loadings of  $\sim 300$ ,  $\sim 500$ ,  $\sim 760$ , and  $\sim 1,570$  torr, respectively.  $P_{\text{Xe}}$  values of  $\sim 41\%$  and  $\sim 28\%$  (with  $\sim 760$  and  $\sim 1,545$  torr Xe loadings) have been measured after transfer to Tedlar bags and transport to a clinical 3 T scanner for MR imaging, including demonstration of lung MRI with a healthy human subject. Long “in-bag”  $^{129}\text{Xe}$  polarization decay times have been measured ( $T_1 \sim 38$  min and  $\sim 5.9$  h at  $\sim 1.5$  mT and 3 T, respectively)—more than sufficient for a variety of applications.

hyperpolarization | laser-polarized xenon | lung imaging | optical pumping

Owing to the detection sensitivity provided by their high, nonequilibrium nuclear spin polarization, hyperpolarized (HP) noble gases (e.g.,  $^{129}\text{Xe}$  and  $^3\text{He}$ ) are used in a number of NMR/MRI applications (1). Human lung imaging (e.g., refs. 2–5) with  $\text{HP}^{129}\text{Xe}$  is of particular interest. Moreover, xenon is soluble in blood (6), other tissues (7, 8), and many biologically compatible liquids (9), and its proclivity for interacting with other substances and its wide chemical shift range make  $\text{HP}^{129}\text{Xe}$  a sensitive NMR probe of molecular and material surfaces (1, 10–12). In many applications,  $\text{HP}^{129}\text{Xe}$  can replace  $^3\text{He}$ , and the relative abundance of  $^{129}\text{Xe}$  can greatly reduce the impact of the worldwide  $^3\text{He}$  shortage (13) in these instances. Despite considerable progress (14–22), a major obstacle toward implementing  $\text{HP}^{129}\text{Xe}$  for clinical imaging has been the ability to reliably and inexpensively produce large quantities of  $\text{HP}^{129}\text{Xe}$  with high polarization ( $P_{\text{Xe}}$ ).  $\text{HP}^{129}\text{Xe}$  is usually created via spin-exchange optical pumping (SEOP) (23), whereby the unpaired electronic spins of an alkali metal vapor (e.g., Rb) are polarized via optical pumping with circularly polarized light, and the polarization is transferred to noble gas nuclear spins during collisions. It is generally anticipated that high  $P_{\text{Xe}}$  is achievable only in the low xenon-density regime (18,

24), because (i) higher Xe densities increase the destruction of Rb polarization from nonspin-conserving collisions at a rate that is orders of magnitude worse than those of other gases like  $\text{N}_2$  and He (25–27); and (ii) higher total pressures tend to quench the three-body van der Waals contribution to Rb-Xe spin exchange—leaving the less-efficient two-body term (18, 23). Most large-scale polarizers, in particular all that are available commercially, operate in this low-Xe density regime. Applied research with  $\text{HP}^{129}\text{Xe}$  is severely hampered owing to a lack of access to expensive proprietary hyperpolarizers, and to stimulate development of  $\text{HP}^{129}\text{Xe}$  applications, we present here a low-cost, “open-source” design.

In our recent work (22, 28, 29) exploring Rb/Xe SEOP under conditions of high resonant laser flux, an inverse relationship was found between the optimal temperature and the in-cell Xe density. This effect was exploited to achieve surprisingly high  $P_{\text{Xe}}$  values at high Xe densities (e.g.,  $\sim 52\%$ ,  $\sim 22\%$ , and  $\sim 11\%$  at 50, 500, and 2,000 torr Xe in a 75-cc cell) with  $<30$  W of laser power (22). Expanding upon these results by over an order of magnitude, our collaboration's first-generation large-scale ( $\sim 1$  L/h)  $^{129}\text{Xe}$  polarizer should enable a variety of clinical, preclinical, and materials magnetic resonance spectroscopy/MRI applications. (Portions of this

## Significance

Lung diseases comprise the third leading cause of death in the United States and could benefit from new imaging modalities. “Hyperpolarized” xenon-129 can overcome the ordinarily weak MRI signals from low-density species in lung space or dissolved in tissue; however, clinical progress has been slowed by the difficulty in preparing large amounts of hyperpolarized xenon with high magnetization, as well as the cost and limited availability of xenon hyperpolarization devices. We describe a unique low-cost “open-source” xenon “hyperpolarizer,” characterize its ability to produce xenon-129 with high magnetization, and demonstrate its utility for human lung imaging.

Author contributions: M.S.R., S.P., M.J.B., E.Y.C., and B. M. Goodson designed research; G.D.M. designed and machined components; P.N., A.M.C., L.L.W., B. M. Gust, N.W., H.N., S.B., I.M., M.D., G.D.M., M.J.B., E.Y.C., and B. M. Goodson performed research; P.N., A.M.C., L.L.W., I.M., M.S.R., E.Y.C., and B. M. Goodson analyzed data; and P.N. and B. M. Goodson wrote the paper.

The authors declare no conflict of interest.

\*This Direct Submission article had a prearranged editor.

<sup>1</sup>Present address: Department of Cancer Systems Imaging, The University of Texas MD Anderson Cancer Center, Houston, TX 77030.

<sup>2</sup>To whom correspondence should be addressed. E-mail: bgoodson@chem.siu.edu.

<sup>†</sup>For spin-1/2 particles, polarization is defined as follows:  $P = (N_{\alpha} - N_{\beta}) / (N_{\alpha} + N_{\beta})$ , where  $N_{\alpha}$  and  $N_{\beta}$  refer to the numbers of spins in the  $\alpha$  ( $m_{S,I} = +1/2$ ) and  $\beta$  ( $m_{S,I} = -1/2$ ) magnetic sublevels; at thermal equilibrium,  $P_{\text{Xe}}$  is only  $\sim 2.85 \times 10^{-6}$  at 3 T and  $\sim 300$  K.

work were presented previously.<sup>‡</sup>) Composed of mostly off-the-shelf components, our automated, modular polarizer is portable, easy to use, and employs an open-source design that is readily implementable in other laboratories. Unlike most clinical-scale Xe polarizers, which typically run in continuous-flow mode, our hyperpolarizer runs in either single-batch or stopped-flow mode in the Xe-rich gas regime (with up to 1,800 torr, or  $\leq 90\%$ , in a 500-cc cell). The design in part negates the usual requirement to cryocollect the HP  $^{129}\text{Xe}$ —a process that otherwise increases the complexity of the device and can lead to losses of spin polarization during HP  $^{129}\text{Xe}$  accumulation, storage, phase transitions (30), and transfer. Four independent methods were used to measure spin polarization, including the following: in situ field-cycled near-IR spectroscopy (28) (to probe Rb electron spin polarization); in situ low-field  $^{129}\text{Xe}$  NMR (calibrated with thermal  $^1\text{H}$  NMR); gas transfer to 47.5 mT for  $^{129}\text{Xe}$  NMR (calibrated with thermal  $^{13}\text{C}$  NMR); and gas transfer and subsequent  $^{129}\text{Xe}$  NMR/MRI using a clinical 3 T scanner. Excellent agreement was observed among these different approaches; taken together, the  $^{129}\text{Xe}$  polarization values reported here represent, by a significant margin, the highest yet achieved at such high Xe densities—and establish the feasibility of attaining near-unity polarization in single batches with HP  $^{129}\text{Xe}$  quantities sufficient for clinical use (demonstrated here with HP  $^{129}\text{Xe}$  lung ventilation maps from a healthy human volunteer). Long  $^{129}\text{Xe}$  polarization lifetimes were obtained in Tedlar bags that are well explained by current relaxation models (24) and that are more than sufficient for gas-phase storage or accumulation necessary for some applications.

## Methods

**XeNA Polarizer.** XeNA, self-contained in a mobile chassis, is composed of a laser system, an electromagnetic coil assembly, a vacuum/gas-handling manifold, on-board optical and NMR spectrometers (and other sensors) for quality assurance (QA) and feedback, and a computer/automation system (Fig. 1A). The optical path (Fig. 1B) begins with a 200-W laser diode array (QPC Lasers) that produces tunable, frequency-narrowed (29) laser output at the Rb D<sub>1</sub> line ( $\sim 794.8$  nm; nominal FWHM,  $\sim 0.27$  nm). The laser beam passes through an optical fiber and expands to 2-inch diameter before collimation and entrance into a polarizing beam-splitter (PBS). The s-polarized beam component ( $<10\%$ ) is reflected 90° and discarded; the main (p-polarized) beam is rendered circularly polarized with a quarter-wave ( $\lambda/4$ ) plate and directed into the oven, which contains a cylindrical glass optical pumping (OP) cell (2" o.d., 9.75", 500 cc) previously coated with a silanizing agent [SurfaSil (Pierce), to slow  $^{129}\text{Xe}$   $T_1$  relaxation] and loaded with  $<200$  mg of Rb. The cell is loaded with a variable Xe/N<sub>2</sub> gas mixture; N<sub>2</sub> helps suppress reemission of unpolarized light from electronically excited Rb (14) and provides additional collision-broadening of the Rb absorption line (31). The laser beam enters/exits through 3-inch antireflection-coated windows. The beam is retro-reflected back through the cell via a 3-inch mirror and directed into the optics assembly, where the PBS reflects the beam into a beam block. The Teflon oven's temperature is controlled via a heated/cooled gas line from a self-pressurized liquid N<sub>2</sub> dewar. The oven resides in a magnetic field provided by a four-coil electromagnet (Acutrán, 23.6" i.d.; nominal fields of 5.26 or 1.46 mT, corresponding to 62.0-kHz resonance frequency for  $^{129}\text{Xe}$  or  $^1\text{H}$ , respectively). The manifold directs gas flow from cylinders containing natural-abundance Xe (26.44%  $^{129}\text{Xe}$ ), isotopically enriched Xe ( $\sim 86\%$   $^{129}\text{Xe}$ ), and N<sub>2</sub> gas, providing desired mixtures up to 2,000 torr. All experiments used naturally abundant  $^{129}\text{Xe}$ , unless otherwise stated. After passing through O<sub>2</sub> getters, the gases are loaded into the OP cell. Following SEOP, the HP  $^{129}\text{Xe}$  mixture is flowed through perfluoroalkoxy (PFA) tubing and a Teflon filter (Millipore Wafergard) to getter any residual Rb before collection in a Tedlar bag. The cells' glass valve has a mechanically actuated Teflon stopcock; the manifold valves are automated pneumatic or solenoid valves, with Teflon surfaces for those downstream of the cell. In situ QA is provided by Ocean Optics HR4000 near-IR and Magritek Kea2 low-field NMR spectrometers. The near-IR spectrometer's fiber is positioned behind the 3-inch mirror; the NMR spectrometer uses a home-built NMR probe/surface

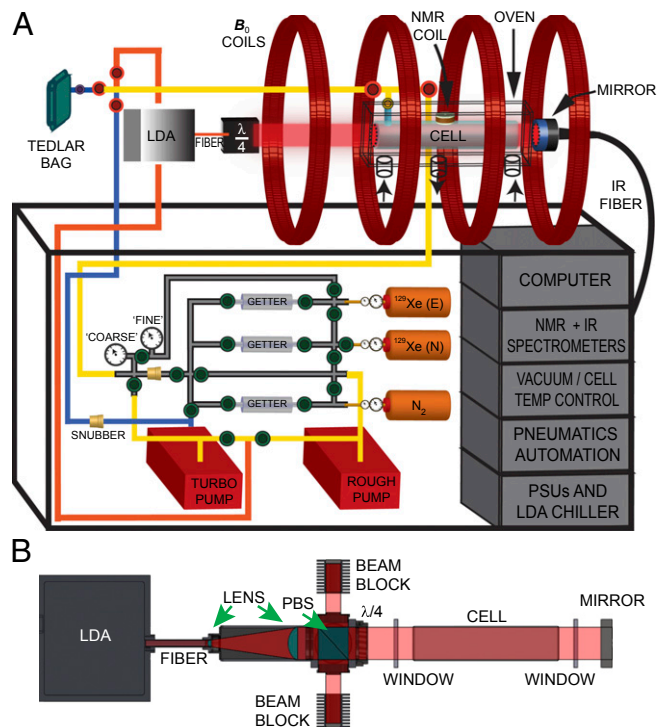


**Fig. 1.** The XeNA polarizer. (A) Schematic of the polarizer's key components (liquid N<sub>2</sub> dewar not shown for clarity). The optical path (shown in B) is represented by (" $\lambda/4$ "). For the gas cylinders, "N" and "E" designate Xe with naturally abundant  $^{129}\text{Xe}$  and isotopically enriched  $^{129}\text{Xe}$ , respectively.

coil. User operation of XeNA employs a GUI programmed in open-source software ([processing.org](http://processing.org)), which drives a microcontroller box that houses the "brain" of the polarizer (Arduino Mega 2560 REV3 microcontroller board), solid-state relays, and a Bürkert manifold enabling pneumatic valve operation. Material costs for the hyperpolarizer were  $<\$125,000$ .

**Other Experimental Aspects.** Xenon was purchased from Nova Gases. MR spectra and images were obtained at 47.5 mT (32) or 3-T field using a Magritek Kea2 with permanent magnet (559-kHz  $^{129}\text{Xe}$  frequency and 508-kHz  $^{13}\text{C}$  frequency) or a Siemens 3-T clinical MRI scanner (34.09-MHz  $^{129}\text{Xe}$  frequency), respectively. Elemental analysis of Tedlar bag contents (following SEOP runs) was performed by Element One to ensure that  $<5.0$  ng of Rb was present in the bag after transfer.

## Results

An estimate of the spatial average of the Rb electron spin polarization,  $\langle P_{\text{Rb}} \rangle$ , can be obtained from measurement of the transmitted light of the pump laser while the magnetic field is cycled (28) (Fig. 2). Spectra are recorded from the laser transmitted through the cell to calculate absorbance values:

$$A = -\ln T = -\ln \left( \frac{I_{\text{hot}}}{I_{\text{cold}}} \right), \quad [1]$$

where  $A$  and  $T$  denote the absorbance and transmittance, respectively, and  $I_{\text{hot}}$  and  $I_{\text{cold}}$  are the integrated intensities of the transmitted laser spectra obtained when a gas-loaded cell is respectively "hot" and "cold" (i.e., with and without significant Rb vapor present). With some simple assumptions, absorbance values may then be compared under the same conditions—except with or without the SEOP magnetic field ( $B_0$ ) on—to calculate an estimate of  $\langle P_{\text{Rb}} \rangle$ , according to a simple relation derived from Beer's Law (28):

<sup>‡</sup>Nikolaou P, et al. (2012) An "open-source"  $^{129}\text{Xe}$  polarizer for clinical imaging, in vivo MRS/MRI, and NMR/MRI of porous materials. *53rd Experimental Nuclear Magnetic Resonance Conference*.

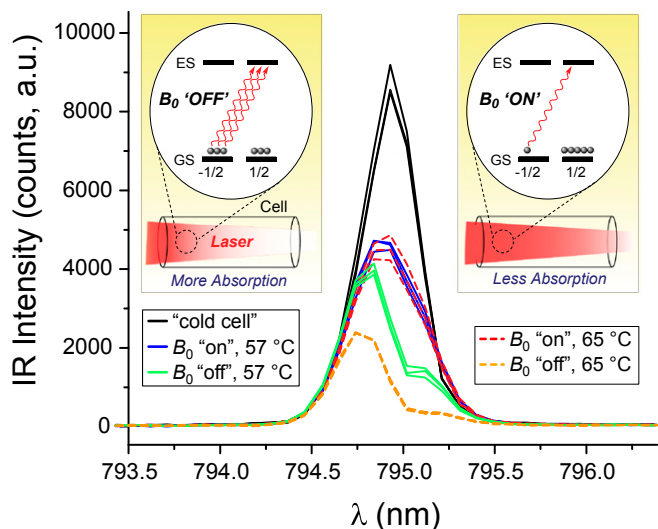


**Fig. 2.** In situ monitoring of Rb electron spin polarization. Near-IR spectra of the pump laser transmitted through the cell at room temperature ("cold cell," black lines); 57 °C and  $B_0 = 5.26$  mT (blue lines); 57 °C and  $B_0 = 0$  mT (green lines); 65 °C and  $B_0 = 5.26$  mT (red dashes); and 65 °C and  $B_0 = 0$  mT (orange dashes). Three scans for each condition are shown; error bars were determined from SDs of spectral integral values. (Insets) The effects of depletion pumping of the Rb vapor on the transmitted laser intensity (assuming  $\sigma^+$  circularly polarized light). When  $B_0$  is "off" (Left), optical pumping is inefficient, resulting in near-equal populations of the ground electronic spin states ( $m_j = +1/2$  and  $-1/2$ ) and a high density of gas-phase absorbers. An applied magnetic field along the quantization axis (provided by the polarized pump laser) results in more efficient optical pumping and unequal ground state populations, corresponding to high electronic spin polarization; the reduced number of atoms in the  $m_j = -1/2$  ground state gives rise to increased laser transmission (Right).

$$|\langle P_{\text{Rb}} \rangle| = \frac{A}{A_0} - 1, \quad [2]$$

where  $A_0$  is the absorbance when  $B_0 = 0$ .<sup>§</sup> Examples of transmission spectra are shown in Fig. 2 for a cell containing 495 and 1,300 torr of Xe and  $\text{N}_2$ , respectively. Multiple near-IR spectra were obtained in rapid succession for each condition, and then averaged and integrated. One set of scans was obtained at 57 °C,  $\sim 10$  min into the SEOP process; the corresponding values of  $\langle P_{\text{Rb}} \rangle$  and  $P_{\text{Xe}}$  measured with low-field NMR (see below) were  $43 \pm 9\%$  and  $48.3 \pm 2.8\%$ , respectively. [ $P_{\text{Xe}}$  cannot be higher than  $\langle P_{\text{Rb}} \rangle$  (Eq. 3); however, the difference between these values is less than the uncertainty.] As part of the optimization process, the temperature of the cell was raised to 65 °C, and after several minutes the sequence was repeated. Improved values of  $\langle P_{\text{Rb}} \rangle$  and  $P_{\text{Xe}}$  of  $71 \pm 6\%$  and  $57 \pm 3\%$ , respectively, were obtained.

Xe polarization was monitored directly via NMR under three different sets of conditions (Figs. 3 and 4). First, low-field  $^{129}\text{Xe}$  NMR can be used to measure  $P_{\text{Xe}}$  within the OP cell. Fig. 3A shows an example of a HP $^{129}\text{Xe}$  NMR spectrum obtained at 5.25 mT from a cell containing 1,545 torr Xe following SEOP and cooldown. Low-field NMR is calibrated using a thermal  $^1\text{H}$  reference signal obtained using the same NMR circuit at the same Larmor frequency of 62 kHz, and tuning/matching conditions

<sup>§</sup>Assumptions include the following:  $\sim 100\%$  circularly polarized light; negligible electronically excited Rb; spatially constant [Rb]; and  $P_{\text{Rb}} \sim 0$  when  $B_0 = 0$  (which ignores effects of weak residual static fields). More precise results may be obtained by applying an orthogonal field during  $B_0 = 0$  scans (or by orienting the polarizer orthogonally to the residual (e.g., Earth's) field).

detecting  $^1\text{H}$  at 1.46 mT from an identical cell filled with 5 mM  $\text{CuSO}_4$ -doped water (Fig. 3B). As part of our initial tests of the Xe-transfer process,  $P_{\text{Xe}}$  measurement was also performed at an intermediate field of 47.5 mT located  $\sim 2$  m from the polarizer. Fig. 3C shows a HP $^{129}\text{Xe}$  NMR spectrum obtained at this field from a portion of HP $^{129}\text{Xe}$  within a cell containing 300 torr Xe following automated transfer to a  $\sim 50$ -cc polypropylene spherical phantom connected to the polarizer via 0.25-inch o.d. PFA tubing and located within the field of the permanent magnet.  $^{129}\text{Xe}$  polarization (here,  $68.7 \pm 3.4\%$ ) was calibrated using a thermal  $^{13}\text{C}$  reference signal obtained from 170 mmol of sodium  $1\text{-}^{13}\text{C}$  acetate in 99.8%  $\text{D}_2\text{O}$  located in an identical phantom (Fig. 3D). Comparison with in situ 5.26-mT  $^{129}\text{Xe}$  NMR polarimetry taken from the OP cell during the same experiment before transferring the gas to 47.5-mT magnet ( $68.5 \pm 3.9\%$ ) indicated no polarization loss within error, and thus a highly efficient HP $^{129}\text{Xe}$  transport process. In future designs, we hope to implement the new approach by Saam and coworkers (33) to measure  $P_{\text{Xe}}$  from corresponding shifts in the optically detected Rb ESR signal.

The hyperpolarizer was delivered to Brigham and Women's Hospital (Boston, MA) and installed adjacent to a clinical MRI suite in February 2012. Optimization of the cell cooldown and automated Xe-transfer processes allowed Xe transfer to Tedlar bags via expansion and subsequent transport to a 3-T clinical MRI. Inset of Fig. 4 shows a high-field HP $^{129}\text{Xe}$  NMR spectrum from a Tedlar bag containing  $\sim 800$  cc of gas (38% Xe by volume, given a cell loading of 760 torr Xe/1,240 torr  $\text{N}_2$ ). The  $P_{\text{Xe}}$  value is calibrated using a thermal  $^{129}\text{Xe}$  NMR signal from a 3-L spherical reference sample containing 4 atm Xe with 86%  $^{129}\text{Xe}$  enrichment and 2 atm  $\text{O}_2$  with a  $T_1$  of 0.99 s. Again, little loss of polarization was suffered throughout the transfer/transport process, given values of  $42.8 \pm 2.4\%$  and  $41 \pm 2\%$  for  $P_{\text{Xe}}$  measured in the cell before transfer and at 3 T in the Tedlar bag, respectively. The latter  $\%P_{\text{Xe}}$  corresponds

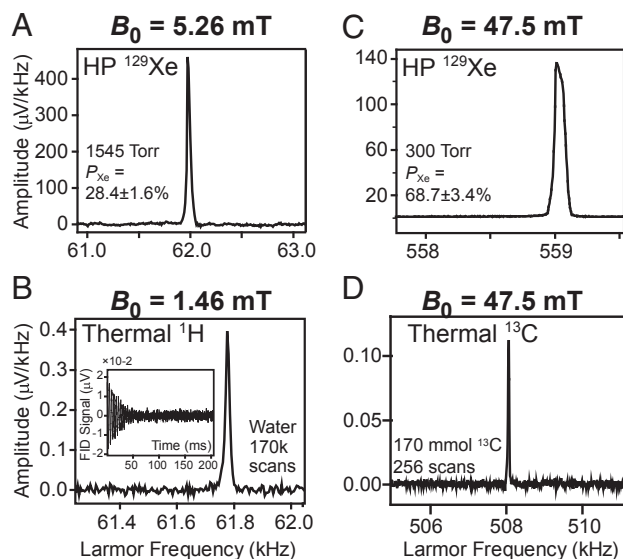


**Fig. 3.** Determination of  $P_{\text{Xe}}$  at low and intermediate magnetic fields. (A) HP $^{129}\text{Xe}$  NMR spectrum from the SEOP cell containing 1,545 torr Xe (and 455 torr  $\text{N}_2$ ) acquired at 5.26 mT (1 scan; 59- $\mu\text{s}$  rf pulse;  $30^\circ$  tipping angle—i.e.,  $\tau_{30^\circ} = 59$   $\mu\text{s}$ ). (B) Reference NMR spectrum from water  $^1\text{H}$  spins (111 M), doped with 5 mM copper sulfate, thermally polarized at 1.46 mT [170,000 scans;  $\tau_{30^\circ} = 16$   $\mu\text{s}$ ; repetition time (TR), 0.3 s;  $P_{\text{H}} = 5.0 \times 10^{-9}$ ]. (Inset)  $^1\text{H}$  free induction decay for the spectrum in the main figure; SNR was used to calculate a relative error bar of 5.7% for  $P_{\text{Xe}}$  values. (C) HP $^{129}\text{Xe}$  NMR spectrum recorded at 47.5 mT (1 scan;  $\tau_{30^\circ} = 18$   $\mu\text{s}$ ) from a 52-mL phantom following transfer of some of the gas (originally 300 torr Xe, 1,700 torr  $\text{N}_2$ ) to the phantom. (D) Reference  $^{13}\text{C}$  NMR spectrum from 170 mmol of sodium  $1\text{-}^{13}\text{C}$  acetate, 14 g in 50 mL of  $\text{D}_2\text{O}$ , also measured at 47.5 mT (256 scans;  $\tau_{90^\circ} = 54$   $\mu\text{s}$ ; TR = 200 s;  $P_{\text{C}} = 4.1 \times 10^{-8}$ ).

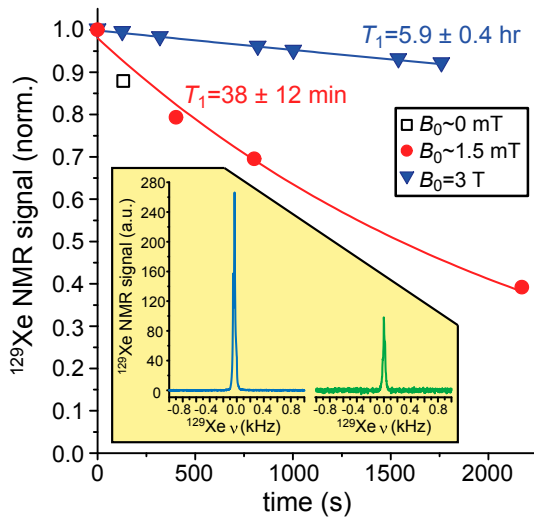


**Fig. 4.** High-field  $^{129}\text{Xe}$  measurements.  $T_1$  decay of  $\text{HP}^{129}\text{Xe}$  NMR signals from Xe gas transferred to Tedlar bags and kept at 3 T throughout the decay (blue triangles) or stored at  $\sim 1.5$  mT (red circles) or  $\sim 0$  mT (white squares) and rapidly transferred to/from 3 T for acquisition. Loss from rf pulsing was negligible (tipping angle,  $<1^\circ$ ). (Inset) (Left) Spectrum from  $\text{HP}^{129}\text{Xe}$  in a Tedlar bag containing  $\sim 800$  cc of gas, 38% Xe by volume following transport to a 3-T clinical MRI (1 scan;  $1.4^\circ$  tipping angle). Gas mixture was nearly identical to main figure. (Right) Reference spectrum from thermally polarized  $^{129}\text{Xe}$  spins in the 3-L spherical phantom containing a Xe/O<sub>2</sub> mixture (32 scans;  $90^\circ$  rf pulses).

to a  $\sim 144,000$ -fold polarization enhancement over the thermal equilibrium value. When preparing multiple bags of HPXe, the total time to produce each bag is  $\sim 35$ – $40$  min, including  $\sim 15$ – $20$  min of SEOP/Xe-polarization time. The final  $^{129}\text{Xe}$  polarization and mole fraction depend on the cell-loading parameters. The strong NMR signals obtained from the  $\text{HP}^{129}\text{Xe}$  gas allowed the polarization decay to be monitored under a variety of conditions. Fig. 4 shows  $^{129}\text{Xe}$   $T_1$  relaxation data for  $\text{HP}^{129}\text{Xe}$  in Tedlar bags recorded at 3 T, but stored at different field strengths: following exponential fits,  $T_1$  decay times of  $38 \pm 12$  min and  $5.9 \pm 0.4$  h were observed for  $^{129}\text{Xe}$  gas in Tedlar bags at 1.5 mT and 3 T, respectively. Such long  $T_1$  values bode well for a variety of applications where gas-phase storage and/or accumulation of  $\text{HP}^{129}\text{Xe}$  is needed (24).

$^{129}\text{Xe}$  polarization values for various Xe densities, operating conditions, and measurement magnetic fields are summarized in Fig. 5A. The data exhibit good run-to-run and method-to-method agreement across the various measurements for the given Xe cell loadings ( $\sim 300$ – $1,600$  torr), despite the fact that the  $P_{\text{Xe}}$  values were measured at different fields, with different NMR acquisition methodologies, and different thermal reference samples. The data include values for in-cell  $P_{\text{Xe}}$  values of  $90.9 \pm 5.2\%$ ,  $57.1 \pm 3.3\%$ ,  $50.1 \pm 2.9\%$ , and  $33.4 \pm 1.9\%$  measured for Xe loadings of 300, 495, 765, and 1,570 torr, respectively;  $P_{\text{Xe}}$  values of  $41 \pm 1.6\%$  and  $28 \pm 1.1\%$  with  $\sim 760$  and  $\sim 1,545$  torr Xe loadings were obtained following transfer to Tedlar bags and subsequent transport to the 3-T scanner, permitting imaging with high signal-to-noise ratio (SNR) ( $\sim 40$ ) to be demonstrated (Fig. 5A, Inset). Moreover, these posttransfer values are  $\sim 2.7$  times greater than previous bests in  $P_{\text{Xe}}$  achieved near such high Xe densities; when combined with the increase in cell volume, these results constitute a  $\sim 18$ -fold improvement in  $\text{HP}^{129}\text{Xe}$  production over the previous best results obtained at such high in-cell Xe densities (22). Finally, recent Food and Drug Administration Investigational New Drug and Institutional Review Board regulatory approval has allowed initial experiments with human subjects to begin. For example, 3D  $\text{HP}^{129}\text{Xe}$  MRI lung ventilation maps (Fig. 5B) and spectra have now been obtained from healthy human

volunteers, demonstrating the utility of the polarizer for a variety of clinical applications.

**Discussion**

The performance of the polarizer is the result of a number of aspects of the SEOP process that are both fundamental and technical in nature (29). SEOP can be treated as a simple relaxation process (23), which at steady state, simplifies to give the following (15):

$$P_{\text{Xe}}(t = \infty) = \frac{\gamma_{\text{SE}}}{\gamma_{\text{SE}} + \Gamma_{\text{Xe}}} \cdot \langle P_{\text{Rb}} \rangle, \quad [3]$$

where  $\gamma_{\text{SE}}$  is the Rb/Xe spin exchange rate and  $\Gamma_{\text{Xe}}$  is the  $^{129}\text{Xe}$  nuclear spin destruction rate ( $=1/T_1$ ); thus, it is convenient to

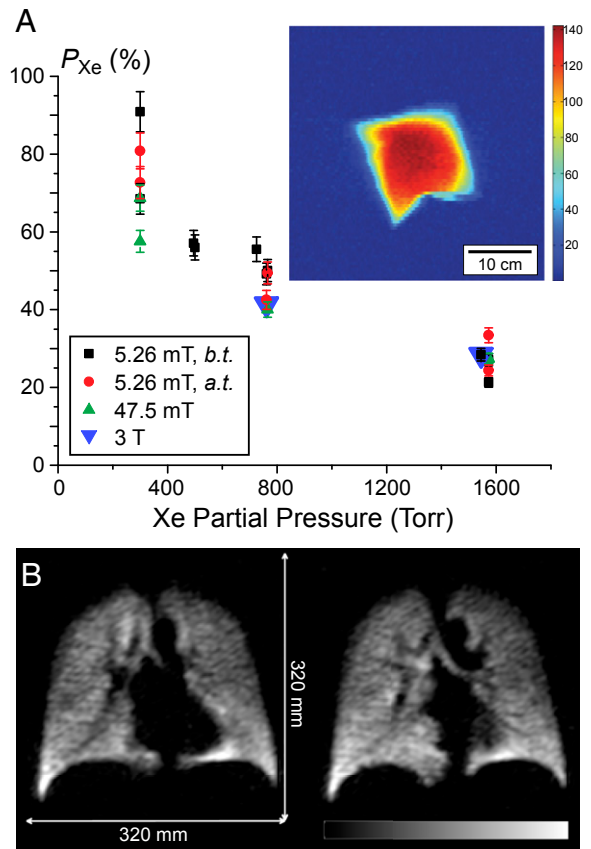


**Fig. 5.** Performance of the XeNA polarizer. (A)  $P_{\text{Xe}}$  values measured at 5.26 mT, 47.5 mT, and/or 3 T, plotted versus Xe pressure before SEOP. Labels “b.t.” and “a.t.” refer to Xe gas remaining in the SEOP cell before and after some was transferred to another container, respectively. Error bars are determined from uncertainties in the spectral integrals obtained from thermally polarized reference samples. The 725-torr value was obtained with 82%-enriched  $^{129}\text{Xe}$ . (Inset) Two-dimensional fast low-angle shot  $^{129}\text{Xe}$  projection image of HPXe in a Tedlar bag following transport to the 3-T MRI [field of view (FOV), 40 cm; slice thickness, 1.7 cm; matrix size,  $80 \times 80$ ; echo time (TE)/repetition time (TR), 2.6/5.1 ms; tipping angle,  $\sim 4^\circ$ ; SNR,  $\sim 40:1$ ]. (B) Two slices selected from a 3D  $^{129}\text{Xe}$  GRE chest image from a healthy human volunteer following inhalation of HPXe from an 800-cc Tedlar bag (filled via expansion from a 500-cc cell containing 1,300 torr HPXe (86%-enriched  $^{129}\text{Xe}$ ) and 700 torr N<sub>2</sub>). Subject performed two respiration cycles (total lung capacity to functional residual capacity), inhaled from bag, and then took a small gulp of air (to help push HPXe out of the trachea); TE/TR, 1.12/11 ms (specific absorption rate-limited); tipping angle,  $6^\circ$ ;  $80 \times 80 \times 14$ ; acquisition time, 4.5 s; FOV,  $320 \times 320 \times 196$  mm<sup>3</sup>;  $2 \times 2 \times 14$  mm digital resolution after zero-filling (SNR  $\sim 8$ – $15$ ). In-cell  $P_{\text{Xe}}$  was 25%, reduced from typical values due to the use of a SEOP cell that had to be thermally regenerated following partial oxidation (during installation).

categorize aspects of the hyperpolarizer and its operation as factors that help optimize  $\langle P_{\text{Rb}} \rangle$ ,  $\gamma_{\text{SE}}$ , and/or  $\Gamma_{\text{Xe}}$ , respectively. First, the most important factor in maximizing global  $\langle P_{\text{Rb}} \rangle$  is the cell illumination by the laser. At a given position ( $r$ ) within the cell, the local  $P_{\text{Rb}}$  is given by the following (15):

$$P_{\text{Rb}}(r) = \frac{\gamma_{\text{OP}}(r)}{\gamma_{\text{OP}}(r) + \Gamma_{\text{SD}}}, \quad [4]$$

where  $\gamma_{\text{OP}}(r)$  is the local OP rate [given by the integrated product of the laser flux and the Rb absorption cross-section (31)], and  $\Gamma_{\text{SD}}$  is the Rb electronic spin destruction rate, which is dominated by nonspin-conserving collisions with Xe [via the spin-rotation interaction (25, 27)] and is high under our conditions because of its proportionality to  $[\text{Xe}]$ . Correspondingly, the laser power used here is also high—usually  $\sim 170$  W, mostly resonant with the Rb  $D_1$  line. In fact, the resonant photon flux is roughly sixfold greater than in ref. 22, but this increase explains only part of the performance improvement. Care was also taken with the optical path to ensure complete illumination throughout the OP cell, with no dark regions, and with additional photon flux provided by retro-reflection. Control of the cell temperature is also key for SEOP optimization. Previously, it was shown that there can be an inverse relationship between Xe density and the optimal temperature for SEOP, where higher  $[\text{Xe}]$  favors lower cell temperatures (22, 29)—an effect that may be explained in part by the need to maintain uniform illumination throughout the cell. Although  $\gamma_{\text{SE}}$  is proportional to the Rb density (34)—ostensibly favoring higher cell temperatures—maintaining a high “photon-to-Rb” ratio (in part by limiting  $[\text{Rb}]$ ) can be particularly important for preserving global  $\langle P_{\text{Rb}} \rangle$  as Xe density is increased, and Xe-induced Rb spin-destruction becomes dominant. [An additional contribution may arise from poor energy dissipation caused by reduced thermal conductivity of Xe-rich mixtures—a possibility we are currently studying with in situ Raman spectroscopy (35).] For example, ongoing simulations predict a high  $\Gamma_{\text{SD}}$  value of  $\sim 134,300 \text{ s}^{-1}$  for the experimental conditions of the 65 °C data in Fig. 2, dominated by Xe collisions (25–27). However, the high resonant photon flux at the front of the cell should give nearly a ninefold greater optical pumping rate ( $\gamma_{\text{OP}} \sim 1.16 \times 10^6 \text{ s}^{-1}$ ); using Eq. 4, such values for  $\Gamma_{\text{SD}}$  and  $\gamma_{\text{OP}}$  would correspond to  $P_{\text{Rb}} \sim 89.6\%$ . Maintaining a relatively low Rb density allows the laser to penetrate efficiently to ensure high photon flux and Rb polarization throughout the cell, consistent with the experimental value ( $\langle P_{\text{Rb}} \rangle = 71 \pm 6\%$ ). Thus, particularly in the limit where  $\Gamma_{\text{Xe}}$  is negligible, maximizing  $\langle P_{\text{Rb}} \rangle$  is more important than  $\gamma_{\text{SE}}$ , once  $\gamma_{\text{SE}}$  is sufficiently high. Indeed, our high  $P_{\text{Xe}}$  values were enabled in part by our ability to achieve long in-cell  $^{129}\text{Xe}$   $T_1$  ( $=1/\Gamma_{\text{Xe}}$ ) decay times. As one example, following SEOP with a cell containing 495 torr Xe and cooldown to 33 °C (where Rb should be condensed), a cell  $T_1$  of  $1.9 \pm 0.6$  h was measured at 5.26 mT. Given a typical build-up time constant measured for one experiment of  $\tau_{\text{OP}} = (\gamma_{\text{SE}} + \Gamma_{\text{Xe}})^{-1} = 8.5$  min, this  $^{129}\text{Xe}$   $T_1$  translates to a spin-exchange rate of  $\gamma_{\text{SE}} \sim 1.8 \times 10^{-3} \text{ s}^{-1}$ —roughly an order of magnitude greater than  $\Gamma_{\text{Xe}}$ . Thus, according to Eq. 3,  $P_{\text{Xe}}$  should closely approach  $\langle P_{\text{Rb}} \rangle$  under these conditions, again in good agreement with the Fig. 2 experiments.

In addition to long HP $^{129}\text{Xe}$  relaxation times measured in OP cells, slow polarization decay was also observed following transfer to Tedlar bags. Generally,  $^{129}\text{Xe}$  relaxation rates are determined by several potential contributions (adapted from ref. 24):

$$\Gamma_{\text{Xe}} = \Gamma_i + \Gamma_g + \Gamma_{\text{O}_2} + \Gamma_w, \quad [5]$$

where  $\Gamma_i$  is an “intrinsic” contribution from spin-rotation interactions of transient and persistent Xe-Xe dimers [ $\Gamma_i = \Gamma_t + \Gamma_p$  (36)],  $\Gamma_g$  results from diffusion through field gradients,  $\Gamma_{\text{O}_2}$  results from dipolar interactions with residual paramagnetic  $\text{O}_2$

in the gas mixture, and ( $\Gamma_w = \Gamma_{w,e} + \Gamma_{w,N}$ ) includes contributions from Xe/wall collisions involving interactions with surface spins of unpaired electrons and nuclei, respectively.  $\Gamma_{w,e}$  can be neglected for Tedlar (polyvinyl fluoride); moreover,  $\Gamma_g$  can be neglected for the 3-T measurements given the homogeneous field. Saam and coworkers recently provided a semiempirical formula for  $\Gamma_i$  that when adapted for our conditions, is given by the following (24):

$$\Gamma_i = \frac{[\text{Xe}]}{56.1\text{h}} + \frac{1}{4.59\text{h}} \left[ 1 + (3.65 \times 10^{-3}) B_0^2 \right] \left( 1 + 0.51 \frac{[\text{N}_2]}{[\text{Xe}]} \right)^{-1}, \quad [6]$$

where the two additive terms respectively correspond to  $\Gamma_t$  and  $\Gamma_p$ ,  $B_0$  is in tesla, the gas densities are in amagat [1 amagat (amg) =  $2.6873 \times 10^{19} \text{ cm}^{-3}$ , the density of an ideal gas at 0 °C and 760 torr], and 0.51 is a factor that takes into account the differential breakup rate of persistent Xe dimers from collisions with  $\text{N}_2$ . Using values for  $[\text{Xe}]$  and  $[\text{N}_2]$  of 0.35 and 0.58 amg, Eq. 6 predicts a limiting value of  $1/\Gamma_{\text{Xe}} = 7.8$  h (with 10% uncertainty), in relatively good agreement with our experimental value of  $5.9 \pm 0.4$  h at 3 T, and indicating effective suppression of other relaxation pathways. Given the expected absence of paramagnetic wall sites, if we assume that (i) relaxation from wall collisions involving surface nuclear spins (37) (e.g.,  $^1\text{H}$ ,  $^{19}\text{F}$ ) is essentially quenched at high field and (ii) that the remaining contribution to  $\Gamma_{\text{Xe}}$  is from residual  $\text{O}_2$  [with a relaxivity of  $\sim 0.4$  Hz/amg (38)], then the differential relaxation rate would correspond to an upper limit for the  $\text{O}_2$  partial pressure of  $\sim 2 \times 10^{-2}$  torr—a reasonable amount. Although  $\Gamma_p$  is the limiting factor for our high-field  $^{129}\text{Xe}$  relaxation, the accelerated decay at 1.5 mT ( $T_1 = 38 \pm 12$  min) is consistent with  $\Gamma_{w,N}$  providing the dominant mechanism. Driehuys et al. (37) showed that, at low field ( $\sim 0$ –10 mT), dipolar relaxation with  $^1\text{H}$  “wall” spins was the primary contributor to  $^{129}\text{Xe}$  polarization decay in cells with organosilane coatings, with  $T_1 < 50$  min at 1.5 mT and 297 K. Although Tedlar may lack the nanoscale Xe permeability of SurfaSil coatings (37), it does possess a high surface density of  $^1\text{H}$  and  $^{19}\text{F}$  spins and likely provides an attractive surface for transient Xe adsorption. More detailed studies of  $^{129}\text{Xe}$  relaxation in Tedlar containers will be the subject of future efforts.

The polarizer’s performance can also be compared with the spin-transfer efficiency,  $\eta$ , defined as follows (adapting from ref. 39):

$$\eta = \frac{P_{\text{Xe}} \cdot N_{\text{Xe}}}{\text{“}T_1\text{”} \cdot \Delta I}, \quad [7]$$

Where  $N_{\text{Xe}}$  is the number of  $^{129}\text{Xe}$  spins,  $\Delta I$  is the photon absorption rate, and “ $T_1$ ” is the  $^{129}\text{Xe}$  relaxation time in hot illuminated cells (taken here as  $\tau_{\text{OP}}$ ). Treated effectively as a constant fundamental to Rb/Xe SEOP,  $\eta$  was found to be  $\sim 0.043$  (39) (i.e.,  $\sim 4.3\%$  of the light angular momentum should end up in  $^{129}\text{Xe}$  spins). Unfortunately, polarizers generally do not approach such efficiency. For example, extrapolating from the prediction of  $\sim 25$  cc-atm/h of 100%-polarized  $^{129}\text{Xe}$  with 1 W of absorbed light, our  $\sim 90$ -W absorption would correspond to  $>2.2$  L-atm/h of 100%-polarized  $^{129}\text{Xe}$ . We can calculate a “production efficiency”,  $\eta'$ , defined as the number of polarized  $^{129}\text{Xe}$  spins produced versus photons absorbed during a SEOP run;  $\sim 0.94$  L-atm/h of  $^{129}\text{Xe}$  spins with  $P_{\text{Xe}} \sim 30\%$  (equivalent to  $\sim 0.28$  L-atm/h of  $P_{\text{Xe}} = 100\%$   $^{129}\text{Xe}$  spins [we assume 1,570 torr Xe, 295 K, SEOP time of 17.5 min, and 100% duty cycle, corresponding to  $\sim 3.5$  L-atm Xe/h gas, with  $P_{\text{Xe}} \sim 30\%$  for the  $^{129}\text{Xe}$  fraction (26.44%)]), gives  $\eta' \sim 0.0054$ . However, if we assume little  $P_{\text{Xe}}$  loss with the use of 100%-enriched  $^{129}\text{Xe}$ , these numbers would climb to  $\sim 1.1$  L-atm/h and  $\eta' \sim 0.021$ , respectively. Although more comparable to the theoretical

limits, these values suggest room for improvement in future designs, and justify further study of fundamental aspects governing SEOP efficiency.

On a technical level, efficiency is aided by the presence of in situ monitoring of the laser absorption and  $^{129}\text{Xe}$  NMR signals, which allow real-time SEOP optimization. Afterward,  $^{129}\text{Xe}$  polarization losses are mitigated by (i) rapid cooldown of the cell while reducing the laser power (to further decrease the heat load, while still providing sufficient Rb illumination—a procedure that allows only a few percent loss of  $P_{\text{Xe}}$ ), as well as (ii) suppressing exposure to  $\text{O}_2$  and other paramagnetic materials throughout the gas lines, (iii) moving the  $\text{HP}^{129}\text{Xe}$  quickly into the sample or transport vessel, and (iv) avoiding Xe phase transitions and other relaxation-susceptible portions of the Xe phase diagram (30). Indeed, Xe cryocollection/sublimation before transfer to the sample is optional for XeNA, but it is normally a requirement with other polarizer designs operating with standard “xenon-lean” gas mixtures. We should add that not cryocollecting the Xe does result in dilution of the  $\text{HP}^{129}\text{Xe}$  with  $\text{N}_2$  gas and leaves behind significant fractions of the SEOP mixture in the cell following the expansion process; however, both of these issues can be mitigated, respectively, by using Xe-rich mixtures and by the addition of a large automated gas piston (15) where the cell contents can be expanded into a much larger volume before transfer.

## Conclusion

We have presented results from a ( $\sim 1$  L/h) hyperpolarizer that produces batches of  $\text{HP}^{129}\text{Xe}$  sufficient for clinical use. The

polarizer’s open-source design and automated operation should facilitate implementation of  $\text{HP}^{129}\text{Xe}$  technology into other laboratories and clinical settings. Good agreement was obtained among the four independent methods for characterizing the spin polarization. The ability to achieve high  $P_{\text{Xe}}$  values at high Xe densities, combined with stopped-flow operation, negates the usual requirement of Xe cryoaccumulation and storage, and opens a door to greatly improved polarization efficiency for quadrupolar isotopes (40, 41) (e.g.,  $^{83}\text{Kr}$  and  $^{131}\text{Xe}$ ). Further improvements in design and gas-handling efficiency will be manifested in our second-generation hyperpolarizer (now under development); other possible improvements in SEOP efficiency of the heavy noble gases may exploit Cs (42) or Cs/Rb hybrid SEOP schemes. These results, combined with ultra-long gas-phase polarization lifetimes and recent regulatory approval, bode well for a host of planned clinical applications with human subjects.

**ACKNOWLEDGMENTS.** We thank B. Saam and G. Schrank for helpful conversations, K. Ranta for simulations, E. Koehnemann for glassblowing, and the reviewers for helpful suggestions. N.W. was supported by National Science Foundation (NSF) Postdoctoral Fellowship OISE-0966393; S.B., B. M. Gust, and B. M. Goodson were supported in part by NSF Grants DMR 0852004 and 1157058. This work was funded by National Institutes of Health (NIH) Grant 1R01 HL096471 and Southern Illinois University Office of Sponsored Projects Administration. M.J.B. is supported by the School of Clinical Sciences, University of Nottingham. E.Y.C. thanks the support from NIH/National Cancer Institute Grant 5R00 CA134749-03 and Department of Defense Congressionally Directed Medical Research Programs Era of Hope Award W81XWH-12-1-0159/BC112431. A.M.C. thanks the support from training NIH Grant R25 CA136440.

- Goodson BM (2002) Nuclear magnetic resonance of laser-polarized noble gases in molecules, materials, and organisms. *J Magn Reson* 155(2):157–216.
- Mugler JP, 3rd, et al. (1997) MR imaging and spectroscopy using hyperpolarized  $^{129}\text{Xe}$  gas: Preliminary human results. *Magn Reson Med* 37(6):809–815.
- Leawoods JC, et al. (2001) Hyperpolarized He-3 gas production and MR imaging of the lung. *Concepts Magn Reson* 13(5):277–293.
- Möller HE, et al. (2002) MRI of the lungs using hyperpolarized noble gases. *Magn Reson Med* 47(6):1029–1051.
- Patz S, et al. (2007) Hyperpolarized  $^{129}\text{Xe}$  MRI: A viable functional lung imaging modality? *Eur J Radiol* 64(3):335–344.
- Bifone A, et al. (1996) NMR of laser-polarized xenon in human blood. *Proc Natl Acad Sci USA* 93(23):12932–12936.
- Chen RY, et al. (1980) Tissue-blood partition coefficient for xenon: Temperature and hematocrit dependence. *J Appl Physiol* 49(2):178–183.
- Swanson SD, Rosen MS, Coulter KP, Welsh RC, Chupp TE (1999) Distribution and dynamics of laser-polarized  $^{129}\text{Xe}$  magnetization in vivo. *Magn Reson Med* 42(6):1137–1145.
- Acosta RH, Blümler P, Münnemann K, Spiess H-W (2012) Mixture and dissolution of laser polarized noble gases: Spectroscopic and imaging applications. *Prog Nucl Magn Reson Spectrosc* 66(1):40–69.
- Rubin SM, Spence MM, Goodson BM, Wemmer DE, Pines A (2000) Evidence of non-specific surface interactions between laser-polarized xenon and myoglobin in solution. *Proc Natl Acad Sci USA* 97(17):9472–9475.
- Jänsch HJ, Gerhard P, Koch M (2004)  $^{129}\text{Xe}$  on Ir(111): NMR study of xenon on a metal single crystal surface. *Proc Natl Acad Sci USA* 101(38):13715–13719.
- Schröder L, Lowery TJ, Hilty C, Wemmer DE, Pines A (2006) Molecular imaging using a targeted magnetic resonance hyperpolarized biosensor. *Science* 314(5798):446–449.
- Shea DA, Morgan D (2010) *The Helium-3 Shortage: Supply, Demand, and Options for Congress*. Technical Report R41419 (Congressional Research Service, Washington, DC).
- Driehuys B, et al. (1996) High-volume production of laser-polarized Xe-129. *Appl Phys Lett* 69(12):1668–1670.
- Rosen MS, et al. (1999) Polarized  $^{129}\text{Xe}$  optical pumping/spin exchange and delivery system for magnetic resonance spectroscopy and imaging studies. *Rev Sci Instrum* 70(2):1546–1552.
- Ruth U, et al. (1999) Production of nitrogen-free, hyperpolarized  $^{129}\text{Xe}$  gas. *Appl Phys B* 68(1):93–97.
- Zook AL, Adhyaru BB, Bowers CR (2002) High capacity production of >65% spin polarized xenon-129 for NMR spectroscopy and imaging. *J Magn Reson* 159(2):175–182.
- Mortuza MG, et al. (2003) Spin-exchange optical pumping of high-density xenon-129. *J Chem Phys* 118:1581–1584.
- Knagge K, Prange J, Rafferty D (2004) A continuously recirculating optical pumping apparatus for high xenon polarization and surface NMR studies. *Chem Phys Lett* 397(1):11–16.
- Ruset IC, Ketel S, Hersman FW (2006) Optical pumping system design for large production of hyperpolarized. *Phys Rev Lett* 96(5):053002.
- Schrank G, Ma Z, Schoeck A, Saam B (2009) Characterization of a low-pressure high-capacity Xe-129 flow-through polarizer. *Phys Rev A* 80(1):063424.
- Whiting N, et al. (2011) Interdependence of xenon density and temperature on  $\text{Rb}/^{129}\text{Xe}$  optical pumping efficiency at high xenon densities. *J Magn Reson* 208(2):298–304.
- Walker T, Happer W (1997) Spin-exchange optical pumping of noble-gas nuclei. *Rev Mod Phys* 69(1):629–642.
- Anger BC, et al. (2008) Gas-phase spin relaxation of  $^{129}\text{Xe}$ . *Phys Rev A* 78(4):043406.
- Bouchiat MA, Brossel J, Pottier LC (1972) Evidence for Rb-rare-gas molecules from the relaxation of polarized Rb atoms in a rare gas. *J Chem Phys* 56(1):3703–3714.
- Wagshul ME, Chupp TE (1994) Laser optical pumping of high-density Rb in polarized  $^3\text{He}$  targets. *Phys Rev A* 49(5):3854–3869.
- Nelson IA, Walker TG (2001) Rb-Xe spin relaxation in dilute Xe mixtures. *Phys Rev A* 65(1):012712.
- Nikolaou P, et al. (2009) Generation of laser-polarized xenon using fiber-coupled laser-diode arrays narrowed with integrated volume holographic gratings. *J Magn Reson* 197(2):249–254.
- Whiting N, et al. (2012) Using frequency-narrowed, tunable laser diode arrays with integrated volume holographic gratings for  $\text{Rb}/^{129}\text{Xe}$  spin-exchange optical pumping at high resonant laser fluxes and high xenon densities. *Appl Phys B* 106(4):775–788.
- Kuzma NN, Patton B, Raman K, Happer W (2002) Fast nuclear spin relaxation in hyperpolarized solid  $^{129}\text{Xe}$ . *Phys Rev Lett* 88(14):147602.
- Romalís MV, Miron E, Cates GD (1997) Pressure broadening of Rb D-1 and D-2 lines by He-3, He-4, N-2, and Xe: Line cores and near wings. *Phys Rev A* 56(6):4569–4578.
- Coffey AM, Shchepin RV, Wilkens K, Waddell KW, Chekmenev EY (2012) A large volume double channel 1H-X RF probe for hyperpolarized magnetic resonance at 0.0475 T. *J Magn Reson* 220(1):94–101.
- Ma ZL, Sorte EG, Saam B (2011) Collisional  $^3\text{He}$  and  $^{129}\text{Xe}$  frequency shifts in Rb-noble-gas mixtures. *Phys Rev Lett* 106(19):193005.
- Cates GD, et al. (1992) Rb- $^{129}\text{Xe}$  spin-exchange rates due to binary and three-body collisions at high Xe pressures. *Phys Rev A* 45(7):4631–4639.
- Newton H, et al. (2013) Comparative study of in situ  $\text{N}_2$  rotational Raman spectroscopy methods for probing energy thermalisation processes during spin-exchange optical pumping. *Appl Phys B*, 10.1007/s00340-013-5588-x.
- Chann B, Nelson IA, Anderson LW, Driehuys B, Walker TG (2002)  $^{129}\text{Xe}$ -Xe molecular spin relaxation. *Phys Rev Lett* 88(11):113201.
- Driehuys B, Cates GD, Happer W (1995) Surface relaxation mechanisms of laser-polarized  $^{129}\text{Xe}$ . *Phys Rev Lett* 74(24):4943–4946.
- Jameson CJ, Jameson AK, Hwang JK (1988) Nuclear spin relaxation by intermolecular magnetic dipolar coupling in the gas phase— $^{129}\text{Xe}$  in oxygen. *J Chem Phys* 89(7):4074–4081.
- Bhaskar ND, Happer W, McClelland T (1982) Efficiency of spin exchange between rubidium spins and  $^{129}\text{Xe}$  nuclei in a gas. *Phys Rev Lett* 49(1):25–28.
- Stupic KF, Cleveland ZI, Pavlovskaya GE, Meersmann T (2011) Hyperpolarized  $^{131}\text{Xe}$  NMR spectroscopy. *J Magn Reson* 208(1):58–69.
- Cleveland ZI, et al. (2006) Exploring hyperpolarized  $^{83}\text{Kr}$  by remotely detected NMR relaxometry. *J Chem Phys* 124(4):044312.
- Whiting N, Eschmann NA, Barlow MJ, Goodson BM (2011)  $^{129}\text{Xe}/\text{Cs}$  (D1, D2) versus  $^{129}\text{Xe}/\text{Rb}$  (D1) spin-exchange optical pumping at high xenon densities using high-power laser diode arrays. *Phys Rev A* 83(5):053428.